IOP Publishing | Institute of Physics and Engineering in Medicine Physics in Medicine and Biology

Phys. Med. Biol. **59** (2014) 4465–4475 doi:10.1088/0031-9155/59/16/4465

Minimizing the $1/r^2$ perturbation for ideal fluence detectors in small source γ-irradiation fields

Alex F Bielajew

Department of Nuclear Engineering, Radiological Sciences The University of Michigan, 2355 Bonisteel Boulevard Ann Arbor, MI 48109, USA

E-mail: bielajew@umich.edu

Received 23 February 2014, revised 23 May 2014
Accepted for publication 6 June 2014
Published 23 July 2014

Abstract

A technique for analyzing the effect of the geometrical shape of a source or a detector, using a quadrupole expansion, is described herein. It is shown that this method may be exploited to predict, optimize the geometry of a source, or a measurement device, and nearly eliminate, the departure from the $1/r^2$ fall-off characteristic due to irradiation from small sources. We have investigated several simple shapes that have a vanishing Q_2 quadrupole moment: a right circular cylinder with a diameter to depth ratio of $\sqrt{2}$, a cone with a radius to height ratio of unity, and an oblate ellipsoid with a diameter to depth ratio of $\sqrt{3/2}$. These ideal shapes produce optimally small departures in a $1/r^2$ field, nearly mimicking a point-like detector. We have also found a rotationally symmetric shape, intermediate to the other three, that has additionally, a vanishing Q_4, the hexadecapole moment. This geometry further improves the $1/r^2$-perturbation characteristics and has an additional free parameter that may be adjusted to model the ideal cylinder, cone or oblate spheroid.

1. Introduction

This paper studies the relationship of instrument response to γ-radiation, in the measurement regime where the source-to-detector distance is greater than the characteristic dimensions of the measurement device, and of the source. Similar investigations have been undertaken previously on this topic [Kondo and Randolph 1960, Bielajew 1990]. However, both of these papers discuss electron transport across the cavity, while this paper concerns itself with photon transport only, as well as geometrical shape optimization.

The results developed herein may be used to design an instrument, specifically an ionization chamber, that minimizes the $1/r^2$ 'fluence perturbation'. However, the conclusions we reach, may apply to many other kinds of radiation detectors, as well as the geometry of the source.

Fluence [ICRU 2011] is a radiometric quantity that is defined at a point in space. Since practical instruments have a finite sensitive volume and, in principle, an arbitrary geometric shape, their response must be integrated over their sensitive volume to model the instrument's measurement. Therefore, if one assumes that the detector is measuring fluence at the center of its sensitive volume, the actual measurements will show a variation from the anticipated $1/r^2$ response, that is dependent on the shape and composition of the instrument.

This begs the question, 'What is the best detector shape?', the motivation for the current study.

2. Unattenuated primary γ measurements

Consider a measurement of primary unattenuated photon integrated fluence, $\Phi_{\rm M}^{\rm D\leftarrow S}$ in a detector (D)–monochromatic source (S) arrangement.

The average integrated fluence is:

$$\Phi_{\rm M}^{\rm D\leftarrow S}=\frac{N_0}{4\pi}\int_{V_{\rm D}}{\rm d}\,\vec{x}_{\rm D}\rho_{\rm D}(\vec{x}_{\rm D})\int_{V_{\rm S}}{\rm d}\,\vec{x}_{\rm S}\frac{\rho_{\rm S}(\vec{x}_{\rm S})}{|\vec{x}_{\rm D}-\vec{x}_{\rm S}|^2} \tag{1}$$

where N_0 is the number of particles that emanate from the source, $V_{\rm D}$ is the volume of the detector, $\vec{x}_{\rm D}$ is the 3D integration variable over the geometry of the detector, and $\rho_{\rm D}(\vec{x}_{\rm D})$ is a response function of the detector, that, in principle, could have a spatial variability. $V_{\rm S}$, $\vec{x}_{\rm S}$, and $\rho_{\rm S}(\vec{x}_{\rm S})$ have similar interpretations for the source, although $\rho_{\rm S}(\vec{x}_{\rm S})$ would play the role of a specific spatial-dependent activity of the source. The factor $|\vec{x}_{\rm D}-\vec{x}_{\rm S}|^{-2}$ accounts for the $1/r^2$ falloff, between the point of photon emission in the source, to the point of interaction in the detector.

$\rho_{\rm D}(\vec{x}_{\rm D})$ and $\rho(\vec{x}_{\rm S})$ are each normalized so that:

$$1=\int_{V_i}{\rm d}\,\vec{\varepsilon}_i\rho(\vec{\varepsilon}_i)\ \text{ where }\ i={\rm D}\text{ or }{\rm S} \tag{2}$$

Equations (1) and (2) may be used to describe the differential $1/r^2$ falloff in the measurement. Note that (1) is symmetric under the interchange of the detector and source, D⇌S.

We define the centers of position of both the source and detector using:

$$0=\int_{V_i}{\rm d}\,\vec{\varepsilon}_i\vec{\varepsilon}_i\rho(\vec{\varepsilon}_i) \tag{3}$$

If we position the coordinate system at the center of volume of the source, and let $\vec{d}$ be the vector from the center of the source to the center of the detector, (1) becomes:

$$\Phi_{\rm M}^{\rm D\leftarrow S}=\frac{N_0}{4\pi}\int_{V_{\rm D}}{\rm d}\,\vec{\varepsilon}_{\rm D}\rho_{\rm D}(\vec{\varepsilon}_{\rm D})\int_{V_{\rm S}}{\rm d}\,\vec{\varepsilon}_{\rm S}\frac{\rho_{\rm S}(\vec{\varepsilon}_{\rm S})}{|\vec{d}+\vec{\varepsilon}_{\rm D}-\vec{\varepsilon}_{\rm S}|^2} \tag{4}$$

An illustration of the geometry under investigation is given in figure 1

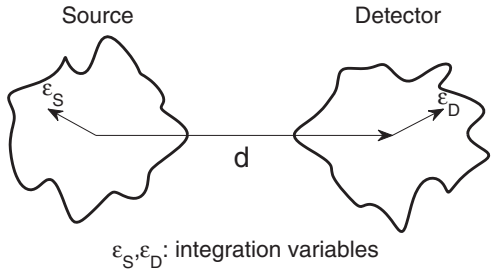

Figure 1. A graphical depiction of the symbols used in (1)–(4).

Borrowing from the language and technique of multipole expansions in electrostatics, we expand (4), assuming $|\vec{\varepsilon}| \ll d$, from which it can be shown that:

$$\begin{aligned}\frac{\Phi_M^{D\leftarrow S}(d)}{[N_0/(4\pi d^2)]} &= \sum_{n=0}^{\infty}\frac{(-1)^n}{d^n}\sum_{k=0}^{n}\binom{n}{k}\frac{2^k}{d^{n-k}}\langle[\hat{d}\cdot(\vec{\varepsilon}_D-\vec{\varepsilon}_S)]^k\,[(\vec{\varepsilon}_D-\vec{\varepsilon}_S)\cdot(\vec{\varepsilon}_D-\vec{\varepsilon}_S)]^{n-k}\rangle \\ &= 1+\frac{Q_2(\vec{\varepsilon}_D)+Q_2(\vec{\varepsilon}_S)}{d^2}+\frac{Q_3(\vec{\varepsilon}_D)+Q_3(\vec{\varepsilon}_S)}{d^3}+\frac{Q_4(\vec{\varepsilon}_D)+Q_4(\vec{\varepsilon}_S)+Q_4(\vec{\varepsilon}_D,\,\vec{\varepsilon}_S)}{d^4} \\ &+\frac{Q_4(\vec{\varepsilon}_D)+Q_4(\vec{\varepsilon}_S)+Q_4(\vec{\varepsilon}_D,\,\vec{\varepsilon}_S)}{d^4} \\ &+\frac{Q_5(\vec{\varepsilon}_D)+Q_5(\vec{\varepsilon}_S)+Q_5(\vec{\varepsilon}_D,\,\vec{\varepsilon}_S)}{d^5}+\mathcal{O}(d^{-6})\end{aligned} \tag{5}$$

The Q_n's are multipole moments, and related to the geometry of the sensitive volume by (5). We note that there is no first order term (the dipole moment), as these have vanished by virtue of locating the endpoints of the $\vec{d}$ at the centers of the source and the detector, as described in (3).

The multipole moments are expressed below in (6), in terms of the longitudinal (‖), with respect to the direction of $\vec{d}$) and lateral (⊥) geometric moments:

$$\begin{aligned}\langle\varepsilon_{i\parallel}^n\rangle &= \int_{V_i} \mathrm{d}\,\vec{\varepsilon}_i\rho(\vec{\varepsilon}_i)\,(\hat{d}\cdot\vec{\varepsilon}_i)^n \\ \langle\varepsilon_{j\perp}^m\rangle &= \int_{V_j} \mathrm{d}\,\vec{\varepsilon}_j\rho(\vec{\varepsilon}_j)\,|\vec{\varepsilon}_j-\hat{d}\,(\hat{d}\cdot\vec{\varepsilon}_j)|^m \\ \langle\varepsilon_{i\parallel}^n\varepsilon_{j\perp}^m\rangle &= \int_{V_i}\mathrm{d}\,\vec{\varepsilon}_i\int_{V_j}\mathrm{d}\,\vec{\varepsilon}_j\rho(\vec{\varepsilon}_j)\rho(\vec{\varepsilon}_i)\,(\hat{d}\cdot\vec{\varepsilon}_i)^n\,|\vec{\varepsilon}_j-\hat{d}\,(\hat{d}\cdot\vec{\varepsilon}_j)|^m\end{aligned} \tag{6}$$

In (6) and following, m and n are integers, $\geqslant 0$.

$$\begin{aligned}Q_2(\vec{\varepsilon}_i) &= 3\langle\varepsilon_{i\parallel}^2\rangle-\langle\varepsilon_{i\perp}^2\rangle \\ Q_3(\vec{\varepsilon}_i) &= -4\langle\varepsilon_{i\parallel}^3\rangle \\ Q_4(\vec{\varepsilon}_i) &= 5\langle\varepsilon_{i\parallel}^4\rangle+\langle\varepsilon_{i\perp}^4\rangle-10\langle\varepsilon_{i\parallel}^2\varepsilon_{i\perp}^2\rangle \\ Q_4(\vec{\varepsilon}_D,\,\vec{\varepsilon}_S) &= 30\langle\varepsilon_{D\parallel}^2\rangle\langle\varepsilon_{S\parallel}^2\rangle-10\langle\varepsilon_{D\parallel}^2\rangle\langle\varepsilon_{S\perp}^2\rangle-10\langle\varepsilon_{S\parallel}^2\rangle\langle\varepsilon_{D\perp}^2\rangle+6\langle\varepsilon_{D\perp}^2\rangle\langle\varepsilon_{S\perp}^2\rangle \\ Q_5(\vec{\varepsilon}_i) &= -6\langle\varepsilon_{i\parallel}^5\rangle+20\langle\varepsilon_{i\parallel}^3\varepsilon_{i\perp}^2\rangle \\ Q_5(\vec{\varepsilon}_D,\,\vec{\varepsilon}_S) &= -60\langle\varepsilon_{D\parallel}^3\rangle\langle\varepsilon_{S\parallel}^2\rangle+20\langle\varepsilon_{D\parallel}^3\rangle\langle\varepsilon_{S\perp}^2\rangle+20\langle\varepsilon_{S\parallel}^3\rangle\langle\varepsilon_{D\perp}^2\rangle-60\langle\varepsilon_{D\parallel}^2\rangle\langle\varepsilon_{S\parallel}^3\rangle\end{aligned} \tag{7}$$

With respect to Q_2, we note that the longitudinal and radial second moments can be arranged, by selection of the geometry of the detector (or source), to cancel each other out, resulting in $Q_2=0$. This fact, proven below in (11), is the major result of this work. The simplest shapes

that realize this are rotationally symmetric (about the $\overrightarrow{d}$ -axis) ellipsoids, right circular cylinders, and double right circular cones, with their bases touching. As demonstrated in the following development, the optimum one-parameter shape is an ellipsoid[1], with its short axis aligned with and centered on the $\overrightarrow{d}$ line, with a long axis to short axis ratio of $\sqrt{3/2}$. A cylinder[2] with its flat face perpendicular to and centered on the $\overrightarrow{d}$ line can be designed so that its $Q_2=0$, if $D/L=\sqrt{2}$, where D is its diameter, and L is its length. The ideal cone has $a=1$. The ideal ellipsoid has a much smaller magnitude of Q_4, compared to the two other ideal shapes.

We also studied another geometry, that we named the 'cyllipsoid', with an additional parameter that allows its surface to obtain the shape of a sphere, an arbitrary ellipsoid, as well as a cylinder. As will be demonstrated in the next section, the two parameters of the cyllipsoid may be chosen to eliminate Q_4 as well.

2.1. An investigation of several geometrical shapes

In this section we present the details of several shapes, all rotationally symmetric with respect to the source-to-detector axis. We restricted the investigation to a pure point source, $\rho_S(\overrightarrow{\varepsilon_S})=\delta(\overrightarrow{x}-\overrightarrow{\varepsilon_S})$, and a detector that measures integrated fluence, $\rho_D(\overrightarrow{\varepsilon_D})=1/V_D$, with the application of ionization chambers in mind.

Equation (4) simplifies to:

$$\Phi(d)=\frac{N_0}{4\pi}\frac{1}{V}\int_V \mathrm{d}\overrightarrow{x}\frac{1}{|\overrightarrow{d}+\overrightarrow{x}|^2} \tag{8}$$

The 5 shapes studied were:

Type	**Equation of surface**	**Parameters**
Sphere	$S_{\text{sphere}}(R)=r^2-R^2=0$	R: spherical radius $r^2=x^2+y^2+z^2$
Right circular cylinder	$S_{\text{cylinder}}(R,a)=\rho^2-R^2=0$ $-R/a\leqslant z\leqslant R/a$	R: cylindrical radius $\rho^2=x^2+y^2$ a: eccentricity
Ellipsoid	$S_{\text{ellipsoid}}(R,a)=\rho^2+a^2z^2-R^2=0$	R: radius of ρ a: eccentricity
Cone	$S_{\text{cone}}(R,a)=\rho+a\lvert z\rvert-R=0$	R: radius of ρ a: eccentricity
Cyllipsoid	$S_{\text{cyllipsoid}}(R,a,b)=\rho^b+a^b\lvert z\rvert^b-R^b=0$	R: radius of ρ a: eccentricity b: 'squareness'

In all cases, $2R$ is the longest interior chord length of the volume, a is the ratio of the longest interior chord length to the shortest, and $b>=2$ is a parameter for the ellipsoid, that models the sphere, the ellipsoid, as well as the cylinder. The surfaces are related by:

$$\begin{aligned}
S_{\text{cyllipsoid}}(R,a,1)&=S_{\text{cone}}(R,a)\\
S_{\text{cyllipsoid}}(R,a,2)&=S_{\text{ellipsoid}}(R,a)\\
S_{\text{cyllipsoid}}(R,a,b\to\infty)&=S_{\text{cylinder}}(R,a)\\
S_{\text{cyllipsoid}}(R,1,2)&=S_{\text{sphere}}(R)\\
S_{\text{ellipsoid}}(R,1)&=S_{\text{sphere}}(R)
\end{aligned} \tag{9}$$

[1] We shall adopt the usual convention in physics that an ellipsoid, refers to a spheroid, and in this particular case, an oblate spheroid.

[2] Similarly, we shall adopt the name 'cylinder', to mean a right circular cylinder, and 'cone', to denote the double cone arrangement.

The spatial moments expressed by (6) are essential to determining the quadrupole moments[3]. They are

$$\begin{aligned}
\langle \varepsilon_{i\|}^{n}\varepsilon_{j\perp}^{2m}\rangle_{\text{sphere}}(R) &= R^{(n+2m)}\frac{3\Gamma(m+1)\Gamma\left(\frac{n}{2}+\frac{1}{2}\right)}{\Gamma(n+2m+3)\Gamma\left(\frac{n}{2}+m+\frac{3}{2}\right)}\\
\langle \varepsilon_{i\|}^{n}\varepsilon_{j\perp}^{2m}\rangle_{\text{cylinder}}(R,\,a) &= \frac{R^{(n+2m)}}{a^{n}}\frac{1}{(n+1)(m+1)}\\
\langle \varepsilon_{i\|}^{n}\varepsilon_{j\perp}^{2m}\rangle_{\text{cone}}(R,\,a) &= \frac{R^{(n+2m)}}{a^{n}}\frac{6\Gamma(2m+2)\Gamma(n+1)}{\Gamma(n+2m+4)}\\
\langle \varepsilon_{i\|}^{n}\varepsilon_{j\perp}^{2m}\rangle_{\text{ellipsoid}}(R,\,a) &= \frac{R^{(n+2m)}}{a^{n}}\frac{3\Gamma(m+1)\Gamma\left(\frac{n}{2}+\frac{1}{2}\right)}{\Gamma(n+2m+3)\Gamma\left(\frac{n}{2}+m+\frac{3}{2}\right)}\\
\langle \varepsilon_{i\|}^{n}\varepsilon_{j\perp}^{2m}\rangle_{\text{cyllipsoid}}(R,\,a,\,b) &= \frac{R^{(n+2m)}}{a^{n}(m+1)}f(n,\,m,\,b),
\end{aligned} \tag{10}$$

where

$$f(n,\,m,\,b)\equiv\int_{-1}^{1}\mathrm{d}x\,x^{n}[\,1-|x|^{b}\,]^{2(m+1)/b}\Big/\left(\int_{-1}^{1}\mathrm{d}x\,[\,1-|x|^{b}\,]^{2/b}\right)$$

With the spatial moments given in (10), the quadrupoles may be determined using (7) directly:

$$\begin{aligned}
\frac{\Phi_{\text{sphere}}(d)}{[N_0/(4\pi d^2)\,]} &= 1+\frac{1}{5}\left(\frac{R}{d}\right)^{2}+\frac{3}{35}\left(\frac{R}{d}\right)^{4}+\mathcal{O}[(R/d)^{6}\,]\\
\frac{\Phi_{\text{cylinder}}(d)}{[N_0/(4\pi d^2)\,]} &= 1+\frac{2-a^2}{2a^2}\left(\frac{R}{d}\right)^{2}+\frac{3-5a^2+a^4}{3a^4}\left(\frac{R}{d}\right)^{4}\\
&\quad+\mathcal{O}[(R/d)^{6}\,]\\
\frac{\Phi_{\text{cone}}(d)}{[N_0/(4\pi d^2)\,]} &= 1+\frac{3(1-a^2)}{10a^2}\left(\frac{R}{d}\right)^{2}+\frac{a^4-a^2+1}{7a^4}\left(\frac{R}{d}\right)^{4}\\
&\quad+\mathcal{O}[(R/d)^{6}\,]\\
\frac{\Phi_{\text{ellipsoid}}(d)}{[N_0/(4\pi d^2)\,]} &= 1+\frac{3-2a^2}{5a^2}\left(\frac{R}{d}\right)^{2}+\frac{15-20a^2+8a^4}{35a^4}\left(\frac{R}{d}\right)^{4}+\mathcal{O}[(R/d)^{6}\,]
\end{aligned} \tag{11}$$

In (11) we see directly, that the cylinder's Q_2 may be set to zero by setting $a=\sqrt{2}$, the cone's by setting $a=1$ and the ellipsoid's by setting $a=\sqrt{3/2}$. All the odd Q's vanish owing to the symmetry of these geometries about the $z=0$ plane. (The cyllipsoid will be treated as a special case, below.)

The ideal cylinder, cone and oblate ellipsoid are shown in figure 2

With these optimized values, the quadrupole expansion takes the following form:

$$\begin{aligned}
\frac{\Phi_{\text{cylinder}}(d)}{[N_0/(4\pi d^2)\,]} &= 1-\frac{1}{4}\left(\frac{R}{d}\right)^{4}+\mathcal{O}[(R/d)^{6}\,]\\
\frac{\Phi_{\text{cone}}(d)}{[N_0/(4\pi d^2)\,]} &= 1+\frac{1}{7}\left(\frac{R}{d}\right)^{4}+\mathcal{O}[(R/d)^{6}\,]\\
\frac{\Phi_{\text{ellipsoid}}(d)}{[N_0/(4\pi d^2)\,]} &= 1+\frac{4}{105}\left(\frac{R}{d}\right)^{4}+\mathcal{O}[(R/d)^{6}\,]
\end{aligned} \tag{12}$$

[3] The expressions are for even n only. The odd-n moments vanish due to the symmetry of the shapes about the $z=0$ plane.

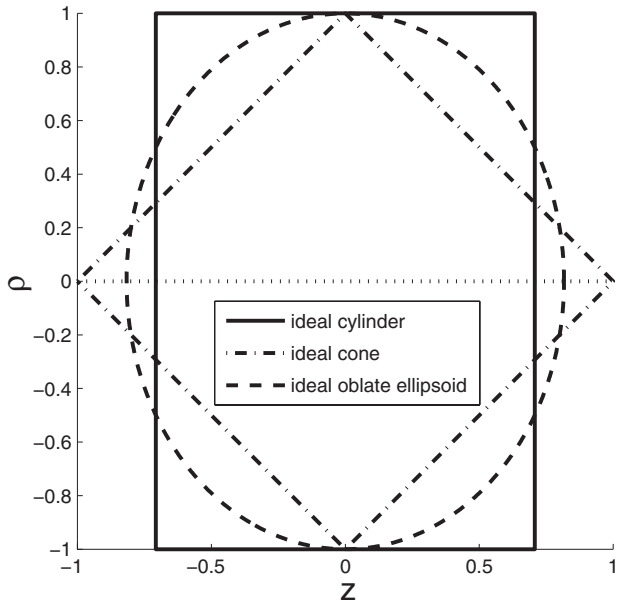

Figure 2. Two dimensional representations of the optimum shapes. These shapes are all rotationally symmetric about the horizontal axis.

Note that the Q_4 for the ideal ellipsoid is much smaller than that of the ideal cylinder's, and the ideal cone's. Additionally, the cylinder's Q_4 has a negative sign, opposite to the positive sign of the two others. This suggests that an intermediate shape could be made to have its Q_4 vanish, motivating the development and investigation of the 'cyllipsoid'.

2.1.1. Optimizing the parameters for the cyllipsoid. This section describes the procedure used to determine the optimum shape parameters, a and b.

The last equation in (10) demonstrates that the functional dependence of the spatial moments depends very simply on R and a. This allows a simple prescription for determining the optimum parameters.

Combining (10) with (7) yields a functional relationship between a and b arising from requiring that $Q_2 = 0$, namely:

$$a_0^2(b) = 3f(2,\,0,\,b)\,/\,f(0,\,1,\,b) \tag{13}$$

Figure 3 depicts $Q_2 = 0$ condition, establishing the relationship between a and b.

To choose the optimum value of b, we rewrite Q_4, substituting a_0 for a, using (7), (10) and (13), and search for the b_0 that causes Q_4 to vanish.

$$Q_4[a_0(b)\,,\,b] = 5f(4,\,0,\,b)\,/\,a_0^4(b) - 10f(2,\,1,\,b)\,/\,a_0^2(b) + f(0,\,2,\,b) \tag{14}$$

Equation (14) is shown in figure 4

The result of these computations is that:

$$b_0 = 2.40231 a_0(b_0) = 1.26435 \tag{15}$$

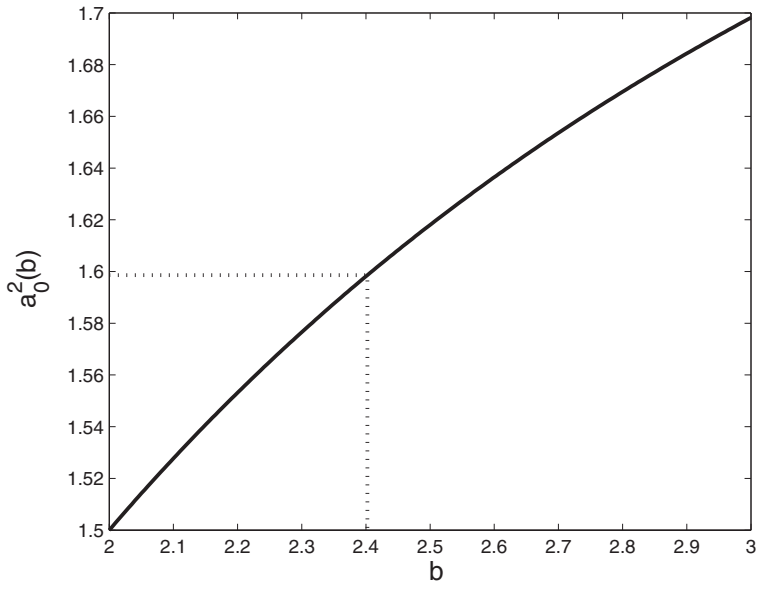

Figure 3. The relationship between the eccentricity parameter, a and the squareness parameter, b, that arises from the requirement that $Q_2=0$. The impulses drawn are obtained from the optimum value of b obtained from the requirement that $Q_4=0$.

The cyllipsoid is shown in figure 5, and contrasted with the oblate ellipsoid, that has the smallest non-vanishing Q_4 among the three other ideal non-cyllipsoidal geometries investigated.

2.1.2. Expressions for the complete physical range of d. In evaluating (8) it is possible to obtain analytic expressions for the sphere, cylinder and ellipsoid, although the cyllipsoid must be left in the form of a single integral that may be evaluated numerically. For brevity, the results are expressed in their integral forms, that were submitted to the symbolic or numerical processing software. In the equations below, $y=R/(ad)$.

$$
\begin{aligned}
\frac{4\pi d^2\Phi_{\text{sphere}}(d)}{N_0} &= \frac{3}{4y}\int_0^1 \mathrm{d}x\; x\log\frac{(1+xy)^2}{(1-xy)^2}\\
\frac{4\pi d^2\Phi_{\text{cylinder}}(d)}{N_0} &= \frac{1}{2(ay)^2}\int_{-1}^1 \mathrm{d}x\log\left(1+\frac{(ay)^2}{(1+2xy+x^2y^2)}\right)\\
\frac{4\pi d^2\Phi_{\text{cone}}(d)}{N_0} &= \frac{3}{2(ay)^2}\int_{-1}^1 \mathrm{d}x\log\left(1+\frac{(ay)^2(1-|x|)^2}{(1+2xy+x^2y^2)}\right)\\
\frac{4\pi d^2\Phi_{\text{ellipsoid}}(d)}{N_0} &= \frac{3}{4(ay)^2}\int_{-1}^1 \mathrm{d}x\log\left(1+\frac{(ay)^2(1-x^2)}{(1+2xy+x^2y^2)}\right)\\
\frac{4\pi d^2\Phi_{\text{cyllipsoid}}(d)}{N_0} &= \frac{1}{y^2}\int_{-1}^1 \mathrm{d}x\log\left(1+\frac{(ay)^2[1-|x|^b]^{2/b})}{(1+2xy+x^2y^2)}\right)\Big/\left(\int_{-1}^1 \mathrm{d}x\,[1-|x|^b]^{2/b}\right)
\end{aligned}
\tag{16}
$$

These results are depicted in figures 6 and 7.

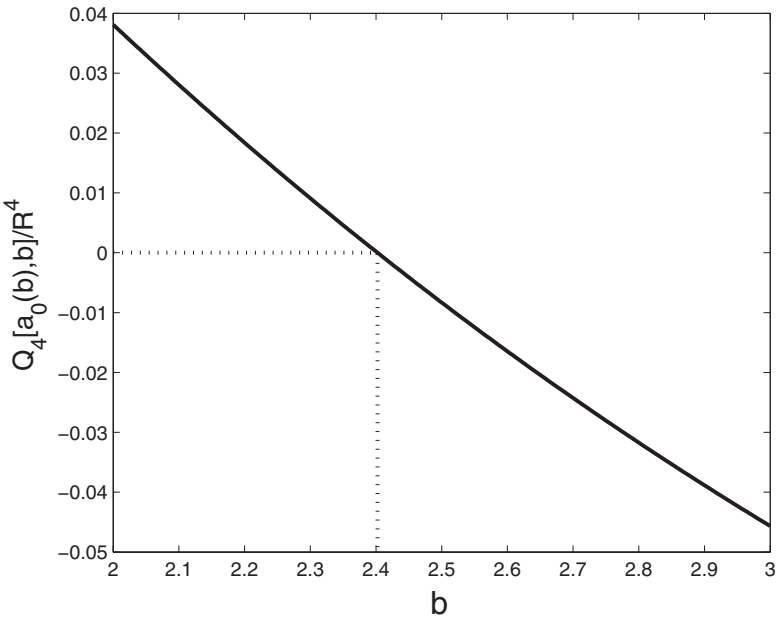

Figure 4. $Q_4[a_0(b), b]$ used to determine the optimum value of $b=b_0$ for the cyllipsoid. At $b=b_0$, and $a=a_0(b_0)$, $Q_2=0$ and $Q_4=0$.

Figure 6 depicts the results of the 'fluence perturbation', $4\pi\, d^2\Phi(d)/N_0$ for the 4 geometries studied, over the entire physical range, from $d\to\infty$ up to $d=R/a$, at which point the source touches the measurement volume. A 'perfect' instrument would measure the fluence at the distance d, with no perturbation. Therefore, the departure from unity represents the amount of the perturbation, due to the finite size of the measurement device. The results for the individual geometries are differentiated in the legend of the figure. Even in the extreme (and impractical) case where the source touches the measurement volume, the perturbation is $+14.45\%$ for the ideal cyllipsoid, $+31.65\%$ for the ideal cone, $+21.64\%$ for the ideal ellipsoid, -12.18% for the ideal cylinder, and $+50\%$ for the sphere.

Figure 7 depicts the perturbation for a typical measurement region. The smallest value of d represented is for $d=10R/a$, about 50cm for a 10 cm diameter spherical chamber. The perturbation for the sphere is $+0.0020$, -9.9×10^{-5} for the ideal cylinder, $+1.4\times10^{-5}$ for the ideal cone, $+8.6\times10^{-6}$ for the ideal ellipsoid and $+7.6\times10^{-8}$ for the ideal cyllipsoid. The curve for the sphere is almost 'off the chart', just visible in the upper left corner in this figure. The curve for the ideal cyllipsoid appears to be completely level, at this magnification. The effect of eliminating quadrupole moments is quite evident!

3. Discussion and conclusions

We have developed a quadrupole technique for analyzing the effect of the geometrical shape of a detector, upon the $1/r^2$-perturbation. The quadrupole expansion technique allows one to characterize the shape of a detector or source in terms of quadrupole moments, similar to the quadrupole expansion technique employed in electrostatics. The parameters of the geometry (radius, or depth) may be adjusted to cause these moments to vanish, resulting in smaller $1/r^2$

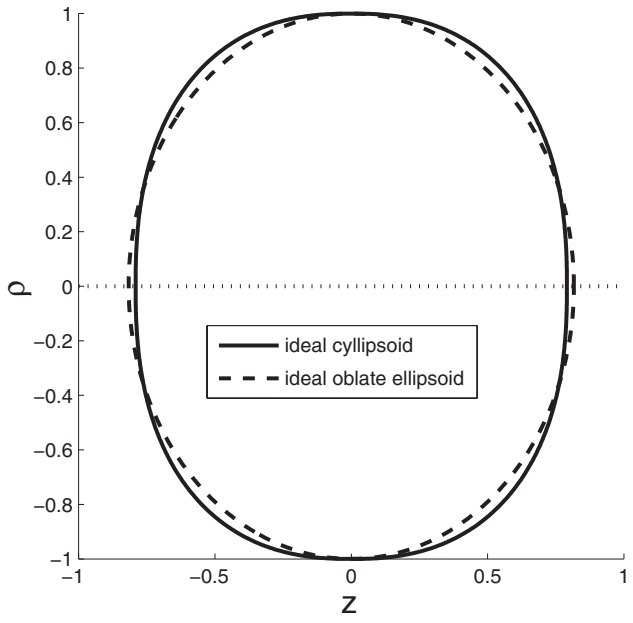

Figure 5. Two dimensional representations of the cyllipsoid and the oblate ellipsoid. They are very close, except the cyllipsoid is somewhat 'squarer'. These shapes are all rotationally symmetric about the horizontal axis.

perturbations that arise from the finite size of the detector or source. We have found three simple shapes that have a vanishing Q_2 moment: a cylinder with a diameter to depth ratio of $\sqrt{2}$, an ellipsoid with a diameter to depth ratio of $\sqrt{3/2}$, and an arrangement of back-to-back cones with a diameter to depth ratio of 1. We have also found another shape, intermediate to the others, that has additionally, a vanishing Q_4.

Such an instrument could be exploited to measure $1/r^2$ variations that arise from other aspects, such as chamber composition, orientation, source shape and size, air scatter and room scatter, as well as electron transport.

The next phase of this study will be to investigate the effect of attenuation and self-scatter due to chamber composition, both analytically, and with Monte Carlo calculations. Once these aspects are fully understood, and the behavior of these chambers characterized completely, the only remaining variables will be source composition, room scatter, and electron transport in the walls of the device. Such an instrument could then be used to research these aspects of the measurement.

An unexplored aspect of this work, is the geometry of the source. The formalism, and the optimization technique developed herein, can be applied to the geometry of the source. This leaves open the intriguing possibility that radiative sources, for example, irradiation capsules or accelerator bremsstrahlung targets, could be further optimized. Another application that may follow from this work is to consider the specific case of line sources, and closer distances, that are germane to brachytherapy dosimetry. The validity of analytic theories [Kondo and Randolph 1960, Bielajew 1990], has recently brought some criticism because of their restriction to point sources [Vianello and de Almeida 2008]. This hypothesis is supported by detailed Monte Carlo calculations [Rodríguez and de Almeida 2004].

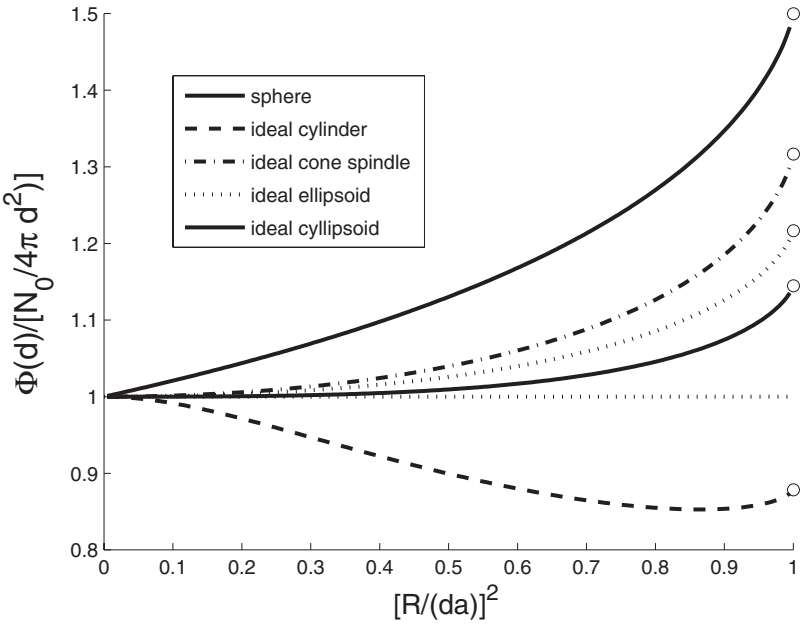

Figure 6. The fluence perturbation for the geometries studied. These values represent all possible measurement distances. The solid line that has the greatest departure from unity is the sphere, while that with the smallest departure is the ideal cyllipsoid. The horizontal line at unity would represent a 'perfect' instrument, with no $1/r^2$ perturbation.

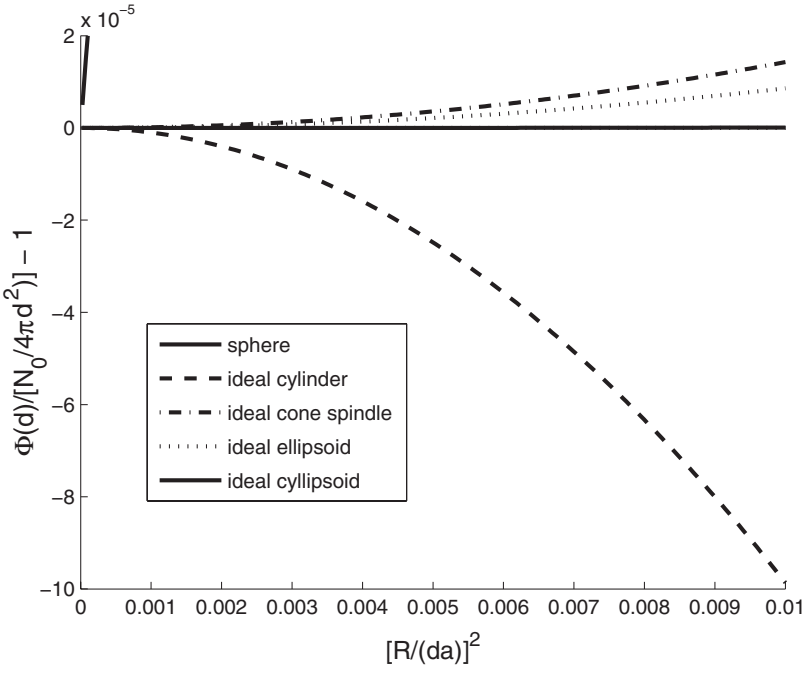

Figure 7. The same data as figure 6 zoomed into a typical measurement region.

Acknowledgments

The hospitality of the Ionizing Radiation Standards Group, at the Institute for National Measurement Standards, National Research Council of Canada, Ottawa, is gratefully acknowledged. Part of this work was performed there, during a sabbatical leave. The lively discussions with E Mainegra-Hing, M McEwen, C Ross and F Tessier were greatly appreciated.

References

Bielajew A F 1990 An analytic theory of the point-source non-uniformity correction factor for thick-walled ionisation chambers in photon beams *Phys. Med. Biol.* **35** 517–38

Kondo S and Randolph M L 1960 Effect of finite size of ionization chambers on measurements of small photon sources *Radiat. Res.* **13** 37–60

Rodríguez M L and de Almeida C E 2004 The photon fluence non-uniformity correction for air kerma near Cs-137 brachytherapy sources *Phys. Med. Biol.* **49** 1705–9

Vianello E A and de Almeida C E 2008 Experimental derivation of the fluence non-uniformity correction for air kerma near brachytherapy linear sources *Med. Phys.* **35** 3389–92

ICRU 2011 Fundamental quantities and units for ionizing radiation *ICRU Report* 85 (Bethesda, MD: ICRU)